



Computer supported toolpath planning for LMD additive manufacturing based on cylindrical slicing

Diego Montoya-Zapata^{1,2,3} · Aitor Moreno¹ · Igor Ortiz³ · Jorge Posada¹ · Oscar Ruiz-Salguero²

Received: 2 June 2023 / Accepted: 14 August 2023 / Published online: 4 September 2023
© The Author(s), under exclusive licence to Springer-Verlag London Ltd., part of Springer Nature 2023

Abstract

In laser metal deposition of overhanging geometries, non-planar layers are used to partially avoid the highly inconvenient support structures. Multi-axis machines provide extra degrees of freedom that allow the deposition of non-planar layers. However, path planning for non-planar slicing is complex because, in most geometries, it encourages non-homogeneous metal deposition among the dispenser paths. For workpieces presenting a direction normal to which all cross sections have non-null common kernel (called here “revolute workpieces”), it is possible to use a cylindrical (i.e., iso-radial) slicing which still enables homogeneous path generation and metal deposition. This manuscript presents the implementation and experimental validation of a path-planner for laser deposition metal dispensers which build revolute workpieces by stacking iso-radial layers. Isometry is preserved between each 3D cylindrical layer and the 2D parametric space (κ, γ) where the dispenser path is planned, so deposited metal density can be homogenized. The path-planner takes advantage of the natural isometry between the (κ, γ) flat surface and the 3D cylinder (due to the cylinder developability). This isometry allows for (i) the application of conventional 2D dispenser path planning for 3D iso-radial layers and (ii) the control of inter-bead distance and dispenser velocity. The implemented path-planner also allows the control of the deposited thickness for each iso-radial layer. To validate experimentally our strategy, we manufacture spur and helical gear teeth on a cylindrical substrate. The results of these experiments show that our strategy generates toolpaths suitable for the manufacturing of industrial workpieces via laser metal deposition.

Keywords Metal additive manufacturing · Non-planar slicing · Laser metal deposition · Computer simulation · Revolute parts

✉ Diego Montoya-Zapata
dmontoya@ikergune.com

Aitor Moreno
amoreno@vicomtech.org

Igor Ortiz
iortiz@ikergune.com

Jorge Posada
jposada@vicomtech.org

Oscar Ruiz-Salguero
oruiz@eafit.edu.co

- ¹ Vicomtech Foundation, Basque Research and Technology Alliance (BRTA), Mikeletegi 57, Donostia-San Sebastian 20009, Spain
- ² Laboratory of CAD CAM CAE, Universidad EAFIT, Cra 49 no 7-sur-50, Medellín 050022, Colombia
- ³ Ikergune A.I.E., INZU Group, San Antolin 3, Elgoibar 20870, Spain

Nomenclature

AM	Additive manufacturing.
B-Rep	Boundary representation of a solid object in \mathbb{R}^3 .
LMD	Laser metal deposition.
(x, y, z)	Convention triplet for Cartesian coordinates.
(θ, ρ, u)	Convention triplet for cylindrical coordinates. θ is the azimuth angle. ρ is the axial distance from the z -axis. u is the height.
(κ, γ, v)	Convention triplet for the coordinates on the parametric space (isometry cylinder-plane). In this space, the planes $v = c$ are isometric to a cylinder in Cartesian coordinates with radius c and axis the z -axis.
$g : \mathbb{R}^3 \rightarrow \mathbb{R}^3$	Function to transform from Cartesian (x, y, z) to cylindrical coordinates (θ, ρ, u) .

$w : \mathbb{R}^3 \rightarrow \mathbb{R}^3$	Function to transform from cylindrical (θ, ρ, u) to parametric coordinates (κ, γ, v) .
$h : \mathbb{R}^3 \rightarrow \mathbb{R}^3$	Function to transform from parametric (κ, γ, v) to Cartesian coordinates (x, y, z) .
$\text{dist}(\mathbf{W}_1, \mathbf{W}_2)$	Euclidean distance between \mathbf{W}_1 and \mathbf{W}_2 .
$\text{dist}_{\text{geod}}(\mathbf{P}_1, \mathbf{P}_2)$	Geodesic distance (arc-length measured on the cylinder surface) between \mathbf{P}_1 and \mathbf{P}_2 .
$\mathcal{M} \subset \mathbb{R}^3$	2-Manifold embedded in \mathbb{R}^3 . Geometry to be manufactured.
$\mathcal{F} \subset \mathcal{M}$	Face of \mathcal{M} that is also a subset of a cylinder.
$\text{Ker}(Q) \subset \mathbb{R}^2$	Kernel of a planar polygon Q . Convex subset of Q from which every point on the boundary of Q is visible.
$M = (V, T)$	Triangular mesh. V and T are the set of vertices and triangles, respectively. Piecewise linear discretization of the 2-manifold \mathcal{M} .
$t > 0$	Layer thickness [mm].
$d > 0$	Step-over distance, i.e., distance between two consecutive deposition lines (beads) (mm).

1 Introduction

Laser metal deposition (LMD) is a metal additive manufacturing (AM) process. In this process, a laser melts metal powder, or wire, and delivers it on top of a metallic substrate. In the industry, LMD is used for repairing and manufacturing high-valued parts [1].

In LMD, it is highly inconvenient to add support structures (common in polymer-based AM). Yet, they are needed to manufacture metal overhangs given certain part orientations. To limit this problem, LMD often involves the use of multi-axis machines that allow the repositioning of the workpiece during fabrication. To fully exploit this kinematic freedom, it is necessary to deposit material on non-planar surfaces. However, the toolpath generation for non-planar surfaces is challenging because it encourages non-homogeneous metal deposition among the dispenser paths, which can lead to manufacturing defects.

In this manuscript, we address the LMD manufacturing of overhanging geometry of revolute workpieces with a 3D kernel. The kernel of a planar polygon Q , $\text{Ker}(Q) \subset Q$, is the convex subset of Q from which every point on the boundary of Q is visible. Formally, $p \in \text{Ker}(Q)$ if for all $q \in \partial Q$, the segment \overline{pq} lies on Q ($\overline{pq} \subset Q$).

Formally, in this manuscript, we address 3D solid geometries B which have a revolute axis L . For these work pieces B ,

there exists a line $L \subset \mathbb{R}^3$ so that L intersects every $\text{Ker}(Q_i)$ ($Q_i =$ flat polygonal cross-section of B , without holes, normal to L). We will call this line L a *revolute axis for B* . Each cross-section Q_i of B should be connected. These conditions guarantee radial access to the borders of B with an LMD dispenser.

Workpieces B exist for which there is no unique L but instead sets of lines L_i (all) parallel, which are revolute lines *for portions* of B . This case, however, will not be discussed in this manuscript.

Our algorithm does not contemplate cases in which the deposition point is near L or on L ($r \rightarrow 0$). This is a ubiquitous limitation, as curve velocities, accelerations, etc., get deformed when $r \rightarrow 0$. Also, substrate heating rates and bead error exponentially increase in metal deposition in such a case. The solution in these cases is to build, without external support and with basic metal deposition (whose layers are normal to L), a basic stem containing L . Then, the cylindrical (i.e., iso-radial) layers devised in this manuscript progressively clad this stem.

Notice that there are revolute bodies (a) which have cross-sections Q_i with holes, causing $\text{Ker}(Q_i) = \emptyset$, or (b) for which there exists no L intersecting all cross-sections Q_i . These conditions do not necessarily exclude the possibility of using cylindrical slicing-based metal deposition. However, in this manuscript, we do not attempt a systematic taxonomy and solution for those cases. A review of the related work on non-planar slicing and toolpath planning for AM follows.

1.1 Slicing for multi-axis additive manufacturing

Multi-axis AM requires specialized slicing algorithms to allow the fabrication of complex geometry without building support structures. Shan et al. [2] and Xu et al. [3] compute, respectively, temperature and geodesic distance scalar fields over the whole volume of the solid. The level surfaces of these scalar fields conform to the non-planar slices. Dai et al. [4] partition the given solid into voxels. Each layer is defined by a sequence of consecutive voxels that can be deposited on top of the previous layers. It requires synchronized 5-axis motions. Montoya-Zapata et al. [5] summarily discuss dispenser path planning for cylindrical slicing-based metal deposition in revolute work pieces. It lacks the mapping of the (κ, γ) parametric space where the tool path is created to the 3D Cartesian space where the metal layer is materialized. It also lacks a CNC simulation or experimental test run.

Ding et al. [6], Etienne et al. [7], and Zhao et al. [8] map (using cylindrical [6, 8] and nonlinear discrete [7] transformations) the solid into a coordinate frame and then perform planar slicing. The resulting non-planar slices are obtained by mapping the planar slices back to the original coordinate system. Xie et al. [9] and Yigit and Lazoglu [10] generate ellipsoidal and spherical slices, respectively. The intersec-

tion between the solid and the surface is performed using the analytic equations of the surfaces (ellipse or sphere). Eisenbarth et al. [11] focus on the fabrication of exhaust manifolds via LMD. The solid is sliced by planes whose normal vector adapts to the curvature of the exhaust manifold.

Some slicing algorithms first decompose the original solid into a sequence of simpler sub-solids and then slice each sub-solid independently from the other. Researchers use the following approaches to perform the model decomposition. Ruan et al. [12], Wu et al. [13], and Xie et al. [9] use 1D abstractions (skeleton) to simplify the geometry of the solid. The branches of the skeleton determine the sub-solids of the decomposition. Ding et al. [14] segment the solid using the surface curvature. The zones of high curvature dictate the places where new sub-solids arise. Gao et al. [15], Wu et al. [16], Xiao and Joshi [17], and Xu et al. [18] use cutting planes to partition the solid. The number of planes and their locations is determined via heuristic optimization algorithms. Gao et al. [15] and Wu et al. [16] minimize the surface area that corresponds to overhanging geometry. Gao et al. [15] use genetic algorithms, and Wu et al. [16] use beam search. Xiao and Joshi [17] and Xu et al. [18] progressively decompose the solid by maximizing the volume of the sub-solid to be extracted.

1.2 Non-planar toolpath planning in additive manufacturing

The algorithms for toolpath planning for 2.5-axis AM are already mature and stable. However, multi-axis slicing algorithms generate curved layers that require new path-planning algorithms ([19]). Calleja et al. [19] show that the toolpath generated by commercial CAM software does not address the main requirements of LMD, such as the preservation of the inter-bead distance. Moreover, the user sometimes must adjust the generated toolpath to avoid unwanted material over-deposition. González-Barrío et al. [20] present and implement a methodology for the hybrid manufacturing of complex components that involves the use of LMD. The methodology integrates planar and non-planar LMD toolpath generation.

Shan et al. [2] and Xu et al. [3] associate a scalar field of the geodesic distance on the curved slice. The path is given by the isolines in this scalar field. Xie et al. [21] first segment the surface based on the local curvature. The trajectory lines in each sub-patch obey the curvature gradient while trying to preserve the step-over distance. Yigit and Lazoglu [10] develop a zig-zag toolpath for spherical slices. The trajectory lines are obtained by intersecting the sphere with a family of parallel planes that cover the sphere. The generated trajectory preserves the step-over distance. Bi et al. [22] generate the trajectory lines by intersecting the surface with planes. The

position and direction of each plane adjust to the curvature of the surface.

Ding et al. [6], Etienne et al. [7], and Zhao et al. [8] use coordinate transformations to perform the path planning in a planar domain and then take it back to the original coordinate system. The disadvantage of these approaches is that the step-over distance in the planar domain is different from the step-over distance in the non-planar original domain. The preservation of the step-over distance is particularly critical in LMD, where the fabricated workpieces are subject to heavy workloads, and the absence of pores is critical for its performance. Dai et al. [23] focus on the path planning for conical surfaces. This path-planning algorithm follows the same strategy by flattening the conical surface, performing the infill on the 2D planar domain, and transforming it back onto the 3D conical surface. However, in this case, the step-over distance is preserved in the transformation from the planar to the conical domain.

Although, in this article, we do not investigate the influence of the cylindrical slicing on the mechanical properties, previous research has shown that the toolpath strategies influence the mechanical properties of the workpieces manufactured using AM. The toolpath pattern ultimately dictates the thermal history and, therefore, the microstructure of the fabricated workpieces ([24]). Monkova et al. [25] perform uniaxial tensile tests on additively manufactured *MSI maraging steel*. Results show that the printing direction affects the yield strength of the printed samples. Alomarah et al. [26] produce auxetic (materials with negative Poisson's ratio) structures using powder bed fusion AM. The results of uniaxial tensile tests on the manufactured structures show that the Poisson's ratio significantly varies with the loading direction.

1.3 Conclusions of the literature review

Multi-axis machines provide kinematic capabilities that allow material deposition on non-planar surfaces. This kinematic freedom allows the AM fabrication of complex geometry without the need for support structures. In this context, slicing and toolpath planning algorithms must be developed in order to exploit the kinematic capabilities of multi-axis machines. Ding et al. [6], Etienne et al. [7], and Zhao et al. [8] transform the given solid onto a new coordinate frame. Then, the solid is sliced with planes, so as in 2.5-axis AM. Planar trajectories are computed and pulled back to the original coordinate system. However, these coordinate transformation functions do not preserve the step-over distance, which is vital in LMD.

In this manuscript, we propose a process planning algorithm for revolute workpieces that (i) slices the geometry into iso-radial layers and (ii) generates a non-planar toolpath that preserves the step-over distance between the deposition tracks on each iso-radial layer. To preserve the step-over dis-

tance, we exploit the fact that the cylinder and the plane are isometric surfaces (i.e., cylinder developability). For every iso-radial slice, we perform the 2D path planning on its corresponding isometric plane, and to obtain the 3D toolpath, we transform the 2D toolpath using a plane-cylinder isometry function. This strategy for iso-radial slicing is integrated into our previously reported industrial LMD process-planning [27]. We validate experimentally our strategy by manufacturing via LMD spur and helical gear teeth on a cylindrical substrate.

The additive manufacturing of almost any workpiece involves the articulation of material science, machining, robotics positioning, surface finishing, thermal treatment, among other processes. This manuscript specifically addresses the geometrical aspect of LMD metal dispenser trajectory generation. Surely, over time, many contributions will pave the way for metal additive manufacturing.

The remainder of this article is structured as follows: Sect. 2 presents our methodology for (i) performing iso-radial slicing and (ii) generating the toolpath on cylindrical surfaces. Section 3 presents the computational and experimental results of applying our methodology to the fabrication of spur and helical gear teeth. Section 4 presents the conclusions and future work.

2 Methodology

We are developing a CAM module in our software that incorporates the (i) iso-radial cylindrical slicing, (ii) toolpath generation on iso-radial slices, and (iii) connection with the LMD machine. This manuscript addresses the tasks (i) and (ii). The strategy presented herein is integrated into our

previously reported industrial LMD process-planning system ([27]).

We implement a method suitable for LMD manufacturing in which the slices are subsets of cylinders. Our method is focused on the manufacturing of overhang geometry of revolute parts. Figure 1 shows examples of workpieces that our method targets. Since the slices that our method generates are not planar, neither is the toolpath. Therefore, our method requires a multi-axis machine to allow the execution of the non-planar trajectory.

Our method, as shown in Fig. 2, has two stages: (i) the generation of the iso-radial cylindrical slices and (ii) the generation of the toolpath. To generate the iso-radial slices, we use coordinate transformation and planar slicing. On the other hand, to generate the toolpath for each iso-radial slice, we use an isometric cylinder-plane parametrization and 2D planar toolpath strategies. The main advantage of the trajectory that we generate is that the step-over distance (measured on the cylinder surface) between adjacent deposition lines can be controlled. Sections 2.1 and 2.2 detail the steps for the iso-radial slicing and the toolpath generation, respectively.

2.1 Iso-radial cylindrical slicing based on coordinate transformation

2.1.1 Problem statement

Given

(i) A 2-manifold \mathcal{M} without boundary embedded in \mathbb{R}^3 ($\mathcal{M} \subset \mathbb{R}^3$). \mathcal{M} must have one face, say \mathcal{F} , that is a subset of a cylinder of radius R and revolute axis A . (ii) Layer thickness $t > 0$.

Fig. 1 Iso-radial cylindrical slicing. Targeted datasets

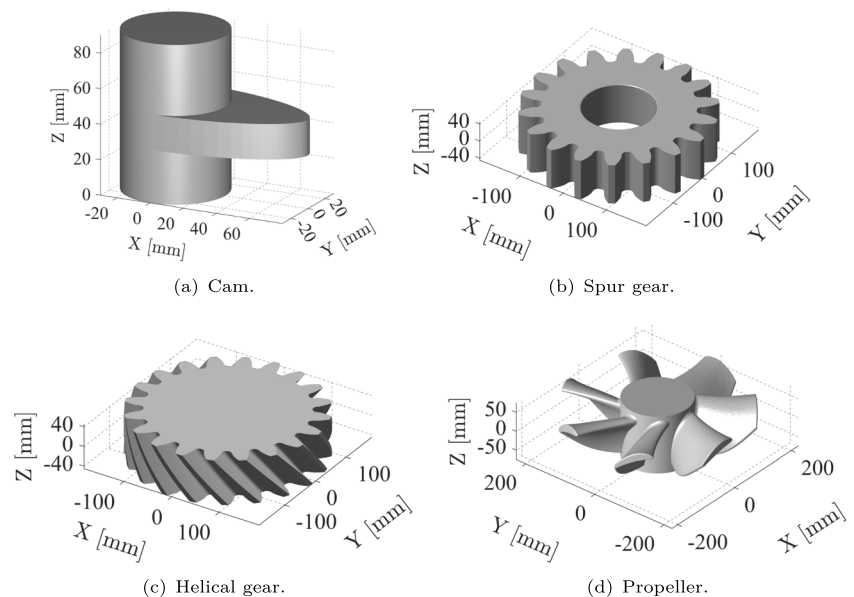
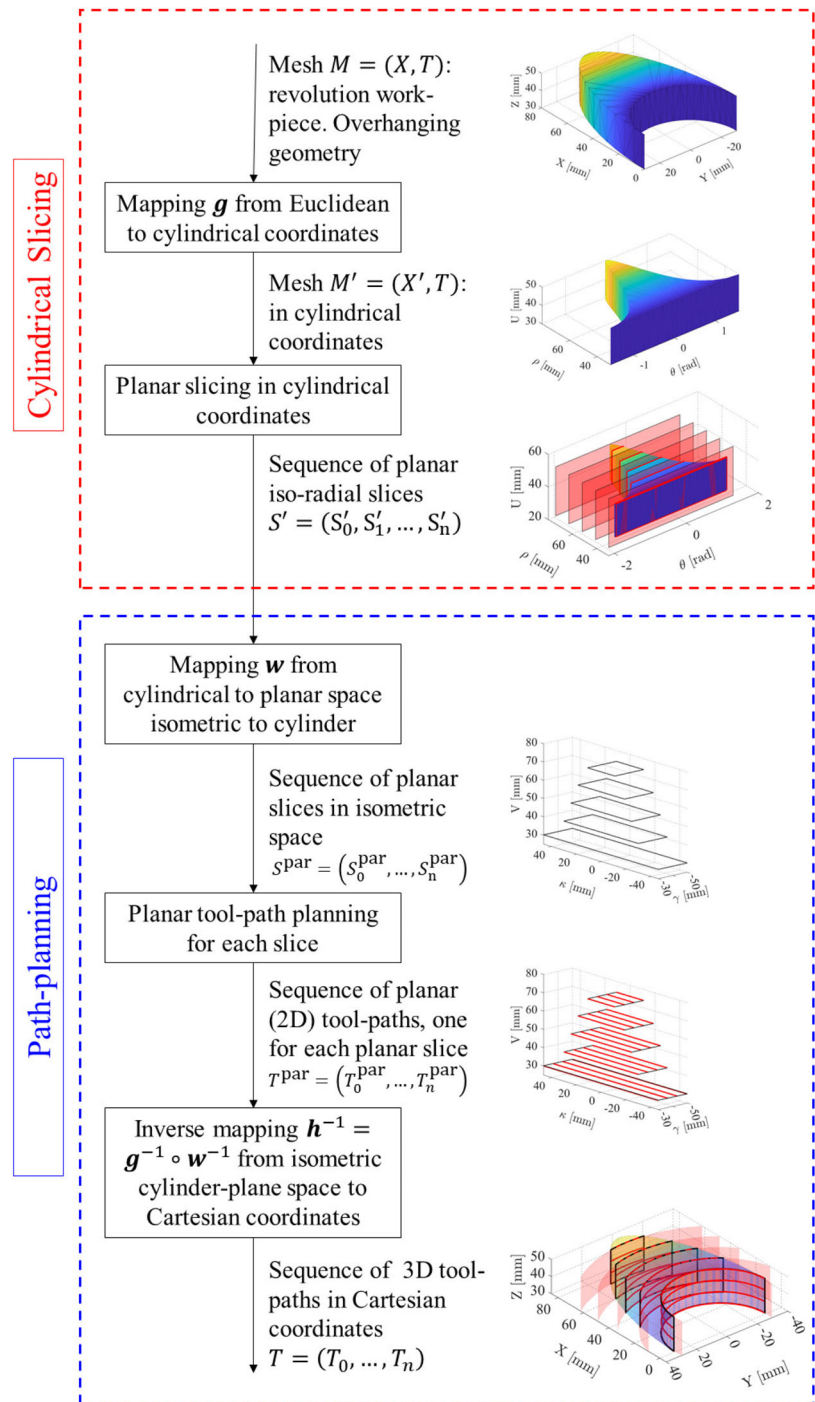


Fig. 2 Workflow for the slicing and toolpath generation



Goal

To slice \mathcal{M} into a sequence S of iso-radial cylindrical slices $S = [S_0, \dots, S_n]$, that is, (i) every slice S_i is a subset of a cylinder of radius $R_i = R + i \cdot t$ and (ii) all the cylinders have the same revolute axis A . If conditions (i) and (ii) are met, the distance between two consecutive slices is equal to the preset layer thickness t .

2.1.2 Generation of the iso-radial slices

In our implementation, we discretize the 2-manifold \mathcal{M} into a triangular mesh $M = (V, T)$, where V and T are the sets of the vertices and triangles, respectively. The steps we follow to perform the cylindrical slicing of the mesh M are as follows (see Fig. 2):

1. Transform the given mesh $M = (V, T)$ in Cartesian coordinates onto the mesh $M' = (V', T)$ in cylindrical coordinates using the function \mathbf{g} in Eq. 1 over the set of vertices V .
2. Perform planar slicing over M' to obtain a sequence of planar iso-radial slices $S' = [S'_0, \dots, S'_n]$. The equation of the plane to obtain the slice S'_i is $\rho = R_i$. The distance between the cutting planes is the layer thickness $t > 0$. In our method, the layer thickness t can also be adjusted for each layer instead of being a constant.
3. To retrieve the corresponding slices $S = [S_0, \dots, S_n]$ in Cartesian coordinates, we apply the inverse map \mathbf{g}^{-1} to S' to transform from cylindrical onto Cartesian coordinates.

Figure 3 shows a graphical description of the procedure applied to the lobe of the cam depicted in Fig. 1. The distance between consecutive clipping planes in Fig. 3d is equal to the distance between consecutive clipping cylinders in Fig. 3e.

2.1.3 Transformation onto cylindrical coordinates

Given a point $\mathbf{P} \in \mathbb{R}^3$ represented in Cartesian coordinates as $\mathbf{P} = (x, y, z)$, the corresponding cylindrical coordinates are given by the function $\mathbf{g} : \mathbb{R}^3 \rightarrow \mathbb{R}^3$:

$$\mathbf{g} \left(\begin{bmatrix} x \\ y \\ z \end{bmatrix} \right) = \begin{bmatrix} \theta \\ \rho \\ u \end{bmatrix} = \begin{bmatrix} \text{atan2}(y, x) \\ \sqrt{x^2 + y^2} \\ z \end{bmatrix}; \tag{1}$$

where the function $\text{atan2} : \mathbb{R}^2 - \{\mathbf{0}\} \rightarrow (-\pi, \pi]$ is the four-quadrant inverse tangent:

$$\text{atan2}(y, x) = \begin{cases} \arccos(x/\rho); & y \geq 0 \wedge \rho > 0 \\ -\arccos(x/\rho); & y < 0 \end{cases} \tag{2}$$

Similarly, if the point \mathbf{P} is initially represented in cylindrical coordinates as $\mathbf{P} = (\theta, \rho, u)$, the corresponding Cartesian

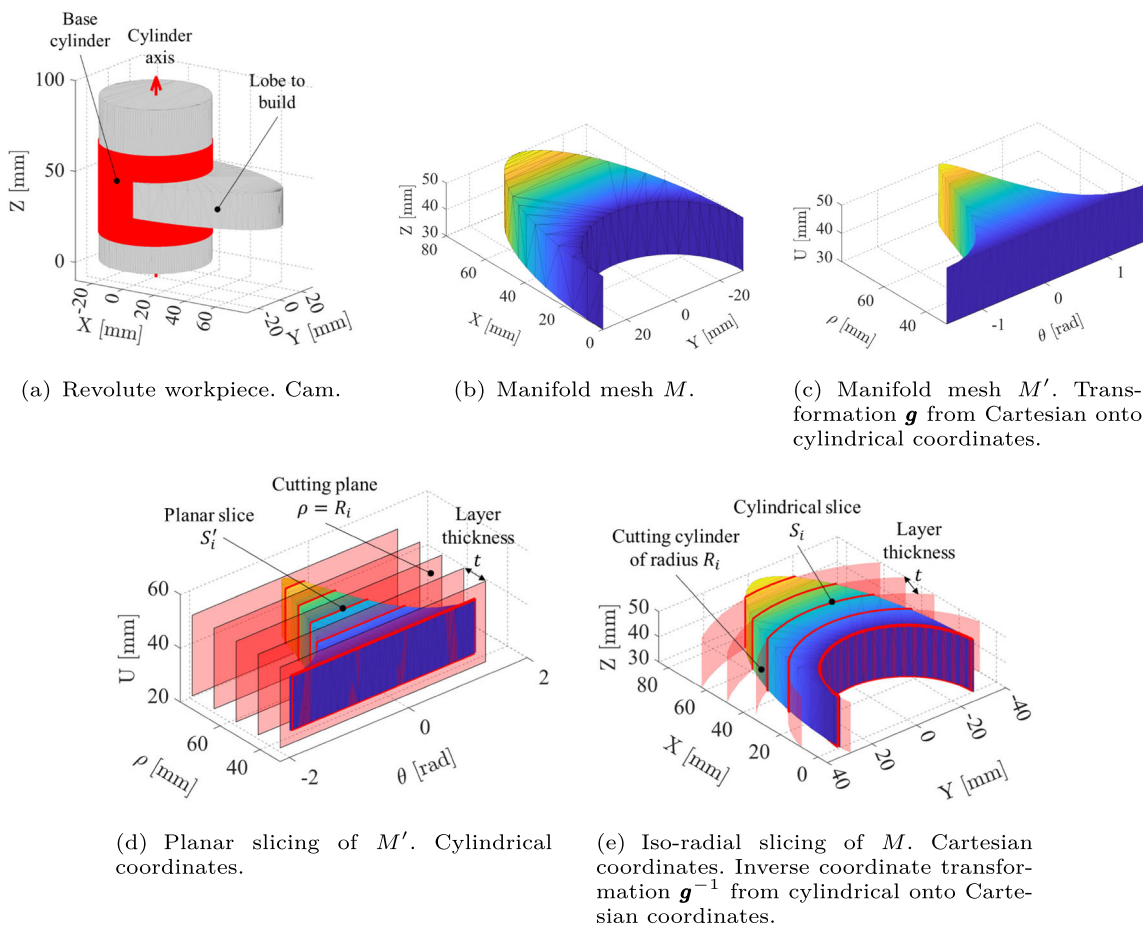


Fig. 3 Iso-radial slicing of revolute workpieces. Detailed steps

coordinates are given by the function $g^{-1} : \mathbb{R}^3 \rightarrow \mathbb{R}^3$:

$$g^{-1} \left(\begin{bmatrix} \theta \\ \rho \\ u \end{bmatrix} \right) = \begin{bmatrix} x \\ y \\ z \end{bmatrix} = \begin{bmatrix} \rho \cos \theta \\ \rho \sin \theta \\ u \end{bmatrix} \tag{3}$$

2.1.4 Planar slicing in cylindrical coordinates

Let C be a cylinder of radius R whose revolute axis is Z :

$$C = \left\{ (x, y, z) : x^2 + y^2 = R^2 \right\}; \tag{4}$$

Notice that $g(C) = C_{\text{cyl}}$ is the following plane in cylindrical coordinates:

$$C_{\text{cyl}} = \{(\theta, \rho, u) : \rho = R\}. \tag{5}$$

We transform the mesh $M = (V, T)$ (in Cartesian coordinates) onto the mesh $M' = (V', T)$ (in cylindrical coordinates) by applying g to the set of vertices V . The intersection between M and the cylinder C in Cartesian coordinates is equivalent to the intersection between M' and the plane C_{cyl} in cylindrical coordinates:

$$g(M \cap C) = M' \cap C_{\text{cyl}} \tag{6}$$

2.2 3D path planning

2.2.1 Toolpath generation for an iso-radial slice

To generate the toolpath for a particular iso-radial slice S_i , we exploit the fact that the cylinder and the plane are isometric surfaces ([28]) (due to the cylinder developability). We generate the toolpath for each iso-radial slice by (1) generating the toolpath on a flat parametric domain (κ, γ) and (2) pulling the 2D toolpath back to the original 3D Cartesian coordinates on the cylindrical surface.

Let $Q_1 = (\theta_1, R, u_1)$, $Q_2 = (\theta_2, R, u_2)$ be two points on the plane $\rho = R_i$ in cylindrical coordinates, such that

$$Q_1 = g(P_1); \quad Q_2 = g(P_2) \tag{7}$$

We apply the additional transformation w to the points Q_1 and Q_2 :

$$w \left(\begin{bmatrix} \theta \\ \rho \\ u \end{bmatrix} \right) = \begin{bmatrix} \kappa \\ \gamma \\ v \end{bmatrix} = \begin{bmatrix} \rho \theta \\ \rho \\ u \end{bmatrix}; \quad w^{-1} \left(\begin{bmatrix} \kappa \\ \gamma \\ v \end{bmatrix} \right) = \begin{bmatrix} \theta \\ \rho \\ u \end{bmatrix} = \begin{bmatrix} \kappa/\gamma \\ \gamma \\ v \end{bmatrix}. \tag{8}$$

We can see that if $W_1 = w(Q_1)$ and $W_2 = w(Q_2)$,

$$\text{dist}_{\text{geod}}(P_1, P_2) = \text{dist}(W_1, W_2) \tag{9}$$

where (i) $\text{dist}(W_1, W_2)$ is the Euclidean distance between W_1 and W_2 , and (ii) $\text{dist}_{\text{geod}}(P_1, P_2)$ is the geodesic distance (arc-length measured on the cylinder surface) between P_1 and P_2 .

To obtain the toolpath in Cartesian coordinates (x, y, z) for an iso-radial slice S_i , we

1. Transform the planar slice S'_i from cylindrical onto parametric coordinates (κ, γ, v) using the function w (Eq. 8). Denote the obtained slice as S_i^{par} . S_i^{par} is isometric to S_i under the function $h = (w \circ g)^{-1} = g^{-1} \circ w^{-1}$. We show this fact in Sect. 2.2.2.
2. Perform 2D planar path planning for the slice S_i^{par} on the parametric (isometry cylinder-plane) space (κ, γ, v) . Denote the obtained toolpath as T_i^{par} .
3. Transform T_i^{par} onto Cartesian coordinates (x, y, z) using the function h . Denote the toolpath in Cartesian coordinates as T_i . The most important characteristic of the function h is that it preserves the step-over distance, that is, the step-over distance between deposition lines in T_i^{par} is the same as in T_i .

Figure 4 shows a graphical description of this procedure to generate the toolpath for the slices of the cam lobe in Fig. 3.

2.2.2 Isometry between the plane and the cylinder

We want to show that h is indeed an isometry (i.e., distance-preserving function). Consider the parametric equation of the plane $\Pi : \gamma = R$, $\Pi : \mathbb{R}^2 \rightarrow \mathbb{R}^3$:

$$\Pi(\kappa, v) = \begin{bmatrix} \kappa \\ R \\ v \end{bmatrix} \tag{10}$$

The first fundamental form of the plane Π , I_Π is

$$I_\Pi = d\kappa^2 + dv^2 \tag{11}$$

Consider the cylinder of radius R centered at the origin parametrized by the function $C : \mathbb{R}^2 \rightarrow \mathbb{R}^3$:

$$C(\theta, u) = g^{-1} \left(\begin{bmatrix} \theta \\ R \\ u \end{bmatrix} \right) = \begin{bmatrix} R \cos \theta \\ R \sin \theta \\ u \end{bmatrix} \tag{12}$$

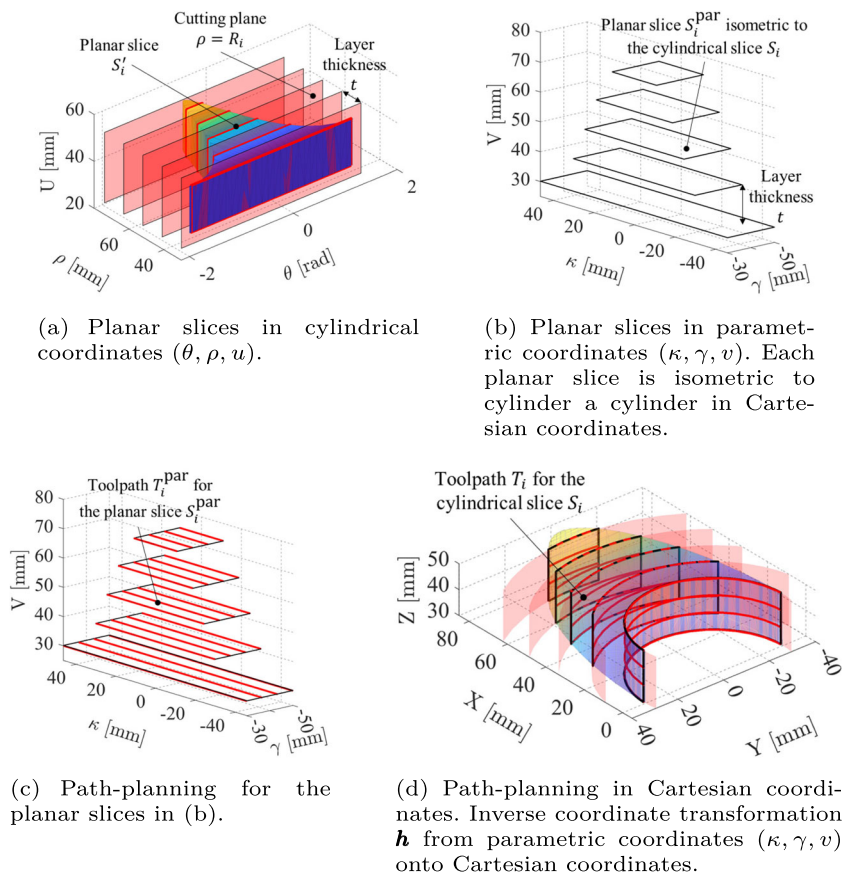
The first fundamental form of the cylinder C , I_C is

$$I_C = R^2 d\theta^2 + du^2 \tag{13}$$

From the definition of w^{-1} in Eq. 8,

$$d\theta = \frac{d\kappa}{R}; \quad du = dv \tag{14}$$

Fig. 4 Iso-radial slicing. Path planning for the resulting iso-radial slices



Replacing into Eq. 13, I_C becomes

$$I_C = R^2 \left(\frac{d\kappa^2}{R^2} \right) + dv^2 = d\kappa^2 + dv^2 \tag{15}$$

which is equal to the first fundamental form of the plane I_Π .

Therefore, for a fixed cylinder radius R , the function $\mathbf{h} = \mathbf{g}^{-1} \circ \mathbf{w}^{-1}$ is an isometry, and, therefore, the plane and the cylinder are isometric.

Since \mathbf{h} is an isometry, it preserves distances. Let $\mathbf{P}_1, \mathbf{P}_2 \in \mathbb{R}^3$ belong to a cylinder of radius R in Cartesian coordinates. Moreover, if $\mathbf{W}_1 = \mathbf{h}(\mathbf{P}_1)$ and $\mathbf{W}_2 = \mathbf{h}(\mathbf{P}_2)$, then

$$\text{dist}_{\text{geod}}(\mathbf{P}_1, \mathbf{P}_2) = \text{dist}(\mathbf{W}_1, \mathbf{W}_2) \tag{16}$$

Figure 5 shows the application of the cylinder-plane isometry to ease the generation of the toolpath for iso-radial

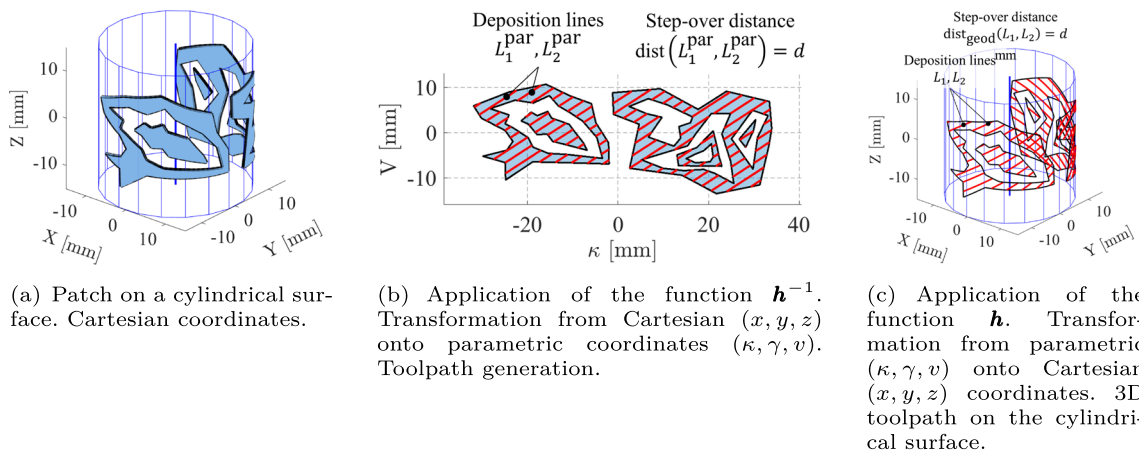


Fig. 5 Path planning for an iso-radial slice. Isometric parametrization. Map between the parametric space (κ, γ, v) and Cartesian coordinates (x, y, z)

slices. Figure 5a shows an example of an iso-radial slice S on a cylinder of radius $R = 10$ mm. We map S onto S^{par} using h^{-1} . Figure 5b shows a planar toolpath generated for S^{par} with step-over distance $d = 2$ mm. Finally, Fig. 5c shows the resulting toolpath in Cartesian coordinates after applying h to the planar toolpath in Fig. 5b. The geodesic distance between the deposition lines on the cylinder is also 2 mm.

2.3 Setup of the LMD system for the experimental validation

Figure 6 shows a picture of the LMD system used for the experimental validation. We use a 6-axis robot mounted on a linear track and an additional vertical rotary plate. We also use a 6000 W high-power laser for the energy input and a coaxial nozzle to deliver the metal powder onto the cylindrical substrate. Table 1 reports the specifications of the LMD system equipment used for the experimental validation of our approach.

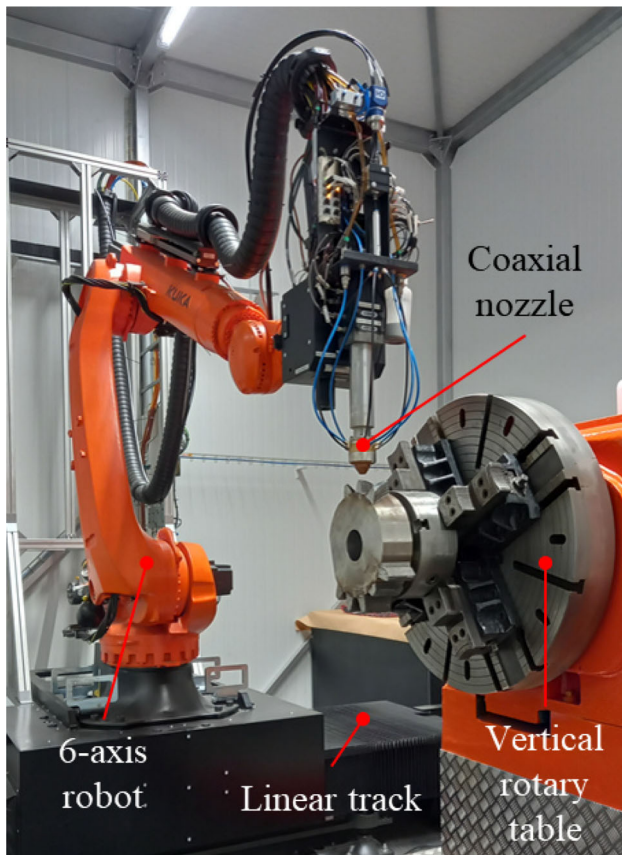


Fig. 6 LMD system used for the experimental validation

Table 1 Experimental set-up. LMD system equipment

Component	Specification
6-axis robot	KUKA KR 210 R3100-2
Linear track	KUKA KL 4000
Rotary axis	Custom vertical rotary plate
Fiber laser	IPG Photonics YLS-6000. Wavelength 1070 nm
Nozzle	Coaxial nozzle designed by Ikerigne A.I.E. Operating powder feed range: 0.33 – 0.83 g/s
Carrier and shielding gas	Nitrogen (N ₂)

3 Results

3.1 Computational results

We conducted numerical simulations with the datasets in Fig. 1. We successfully applied our methodology to perform the slicing and 3D path planning for overhanging features of revolute parts.

Our experiments produce (i) spur gear tooth, (ii) helical gear tooth, (iii) cam lobe, and (iv) propeller blade. Figures 3–4 and 7, 8, 9 present the toolpath generation based on cylindrical iso-radial slicing. Table 2 displays the toolpath-planning parameter values. Notice that the parameters (e.g., t, d) used in the figures for the sake of illustration are not the ones used in the actual LMD manufacturing. These values can be adjusted as required by the particular LMD system or industrial application.

Regarding the generation of iso-radial slices that organically follow the shape of the 3D cylindrical kernel, Figs. 3–4 and 7–9 show that the combination of (i) appropriate coordinate transformation and (ii) planar slicing achieves iso-radial slicing.

Regarding the generation of the 3D toolpath, Figs. 3–4 and 7–9 show the toolpaths obtained using our approach. To show the flexibility of our approach, we defined a different infill angle for each one of the iso-radial slices. In this instance of path generation, we used a hatch pattern. However, any other 2D pattern strategy (e.g., spiral, medial axis-based, continuous zig-zag) can be used. Due to the isometric nature of the cylinder-plane transformation, the step-over distance on the 2D flat layers is the same as on the 3D iso-radial cylindrical layers. These results show the convenience of isometric parametrization in generating 3D trajectories for LMD manufacturing.

Figure 10 shows the full 3D toolpath for the datasets considered in this manuscript. The images in Fig. 10 are obtained from our (under development) software for the pro-

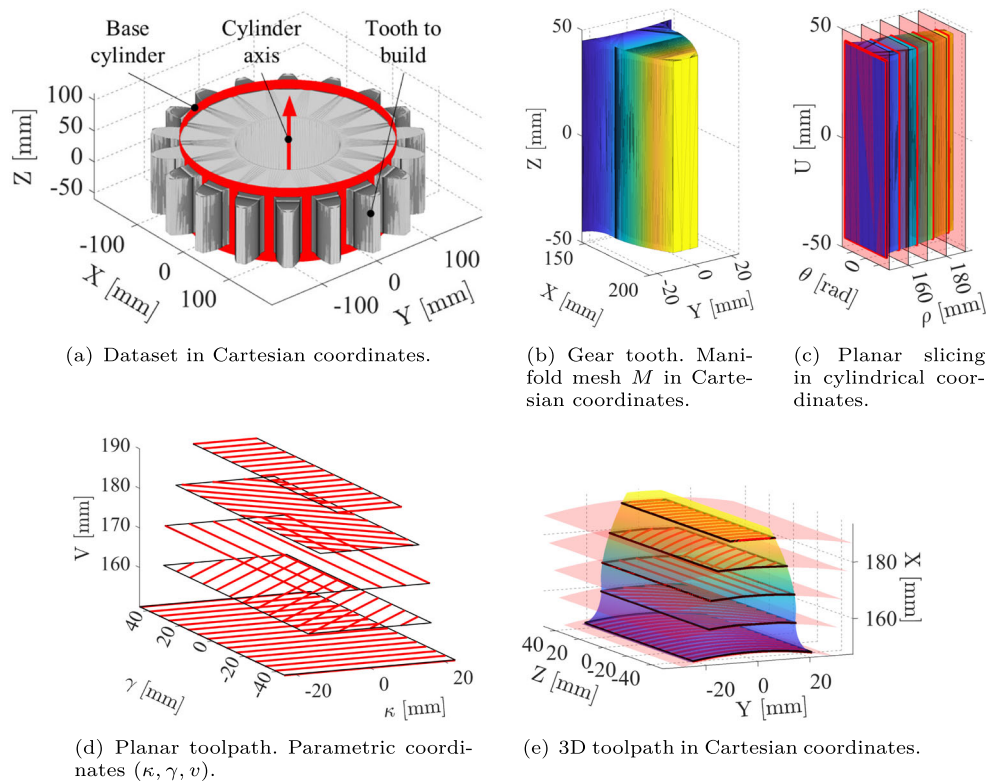


Fig. 7 Spur gear. Iso-radial slicing and toolpath planning

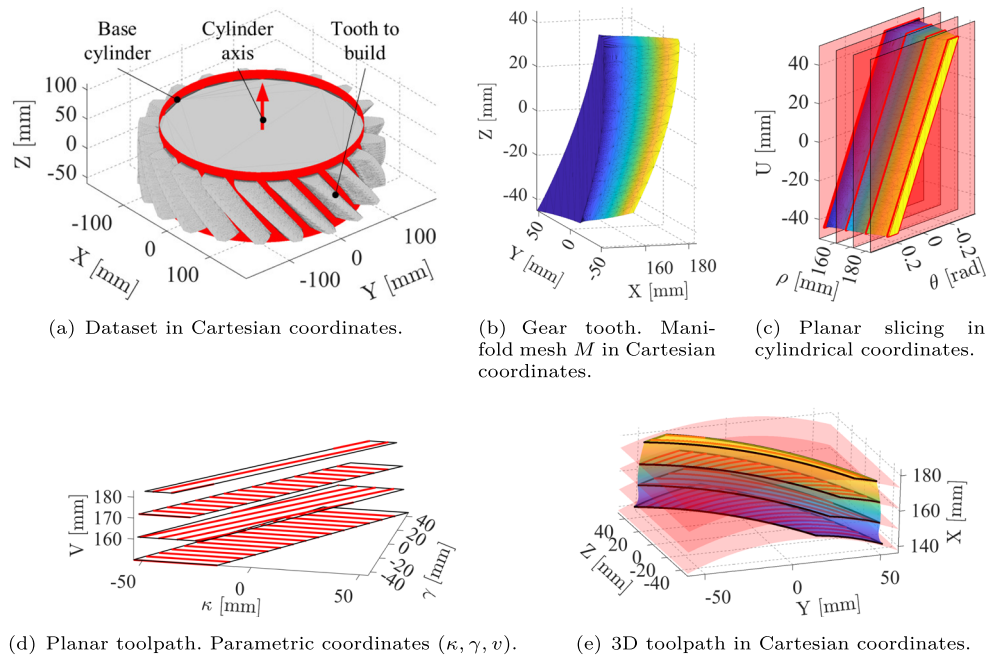


Fig. 8 Helical gear. Iso-radial slicing and toolpath planning

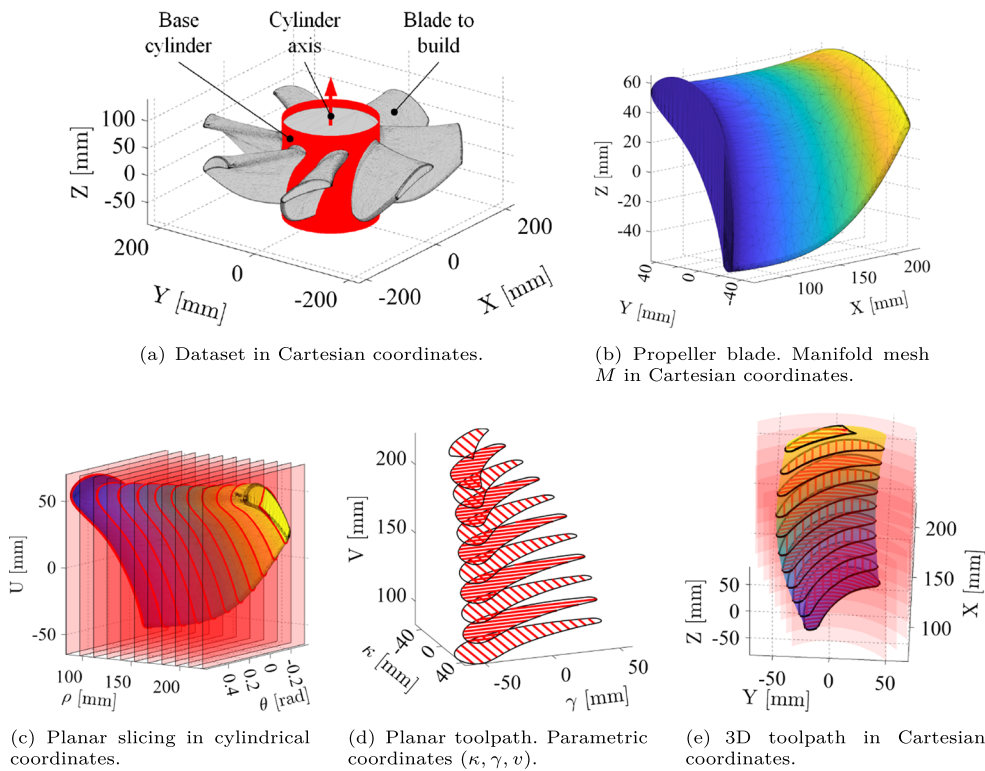


Fig. 9 Propeller. Iso-radial slicing and toolpath planning

cess planning of LMD. The red and blue segments in Fig. 10 describe the laser deposition and laser repositioning trajectories, respectively. The laser repositioning comprises both the repositioning between (i) tracks and (ii) layers. We compute the repositioning trajectories by (i) finding the repositioning trajectory between consecutive planar layers on the parametric coordinates (κ, γ, ν) and then (ii) applying the coordinate transformation function h to obtain the corresponding trajectory in the original Cartesian coordinates.

3.2 Experimental validation

In order to experimentally validate our approach, we manufactured the spur and helical gear teeth in Figs. 7–8 on a cylindrical substrate of radius 150 mm. Table 3 reports the materials and the LMD process parameters used for the experimental validation. To manufacture the teeth, we placed the cylindrical substrate on the vertical rotary plate and used

the coupled movements of the 6-axis robot to execute the piecewise linear toolpaths calculated with our strategy. The rotary plate served as clamp for the cylindrical substrate and also to easily reposition (with asynchronous rotations) the substrate to manufacture each tooth.

Our algorithm does not require the axis of the nozzle to be aligned with the local vector normal to the slice. Previous experiments carried out in our laboratory have shown that it is not necessary to tilt the nozzle if the angle between the gravity line and the surface slice normal vector does not exceed 30° . In this experiment, the nozzle was vertical during the whole deposition process, so the powder dispensing direction was aligned with the gravity line.

Figure 11 shows the iso-radial slices and the full 3D toolpath obtained following our strategy for the manufacturing of the spur and helical gear teeth. Table 4 presents the number of layers needed to manufacture each tooth. The thickness of each layer is uniform ($t = 1.4$ mm as shown in Table 3). For

Table 2 Slicing and path-planning parameters

Dataset	Figure	Layer thickness t (mm)	Step-over distance d (mm)
Cam	Fig. 1a	11.0 mm	6.0 mm
Spur gear	Fig. 1b	10.0 mm	7.0 mm
Helical gear	Fig. 1c	11.0 mm	6.0 mm
Propeller	Fig. 1d	14.0 mm	7.0 mm

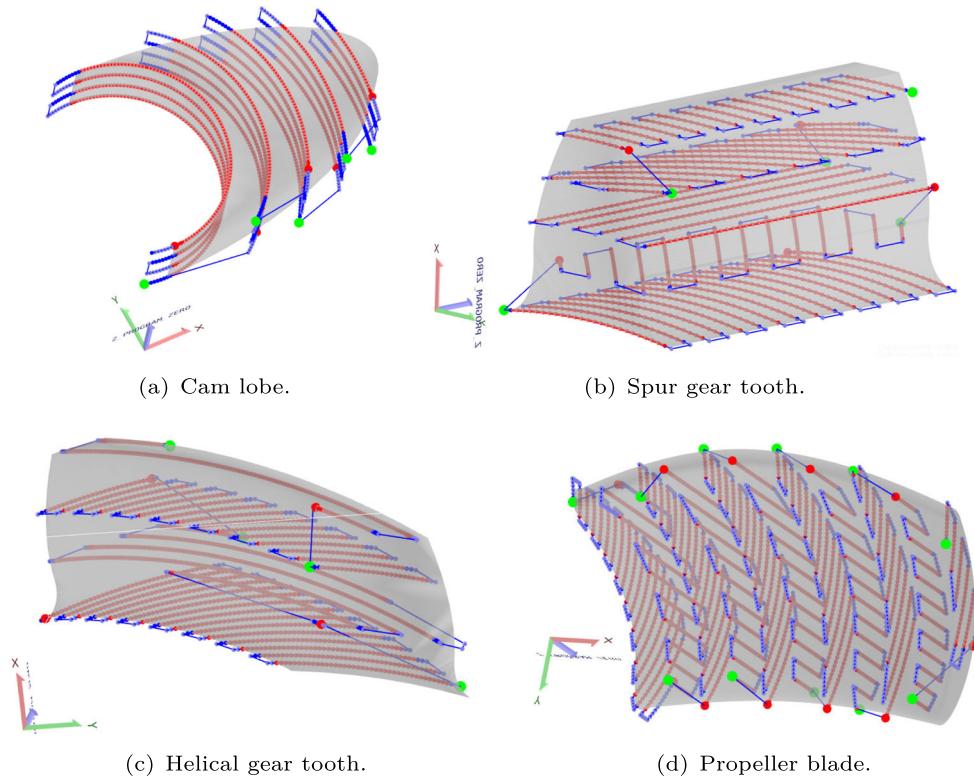


Fig. 10 Full 3D toolpath obtained using our approach. Visualization in our software for LMD process planning. Red segments: deposition. Blue segments: repositioning

each layer, the beads follow the direction given by the tooth flank.

Figure 12 shows pictures of the resulting teeth using our LMD setup. In total, we manufactured 4 spur and 3 helical gear teeth. Each one of the teeth was built independently. Figure 12a shows the manufacturing order of the samples. Table 4 reports the building time for each of the spur and helical gear teeth.

Table 3 Materials and LMD process parameters. Experimental validation. Manufacturing of spur and helical gear teeth

Parameter	Value
Cylindrical substrate	F125 steel
Additive powder	AISI 316L stainless steel
Laser spot diameter	4.9 mm
Tool-head speed	9.0 mm/s
Powder feed rate	0.4 g/s
Carrier gas flow rate	0.075 L/s
Shielding gas flow rate	0.083 L/s
Layer thickness t	1.4 mm
Step-over distance d	3.4 mm
Substrate radius	150 mm

Samples 1–5 and *6–9* display, respectively, to manufacturing experiments of spur and helical gear teeth. *Samples 1–2* and *4–5* correspond to whole spur gear teeth. *Samples 7–9* correspond to whole helical gear teeth. During the deposition of *Sample 3*, we ran out of powder material and did not complete the whole tooth. We also deposited *Sample 6* (the first 3 layers of the helical tooth) before manufacturing a whole helical tooth. This experiment served to check for potential nozzle-workpiece and nozzle-rotary plate collisions.

Figure 12 shows that several samples of the gear teeth were successfully manufactured and that the manufactured teeth accurately represent the expected geometry. These results show the relevance of our method for the LMD manufacturing of overhanging geometry on cylindrical substrates. The main characteristic of our path-planning method is that it allows control of the inter-bead (or step-over) distance on a (non-planar) iso-radial layer. The preservation of the step-over distance is particularly relevant in LMD (and other metal AM processes) as it impacts the quality of the produced workpieces.

The computation of the 3D toolpath for non-planar slices is not trivial, especially if the preservation of the step-over distance between deposition beads is imperative. Our approach is advantageous because it preserves the 3D step-over distance on iso-radial cylindrical layers using (i) well-known

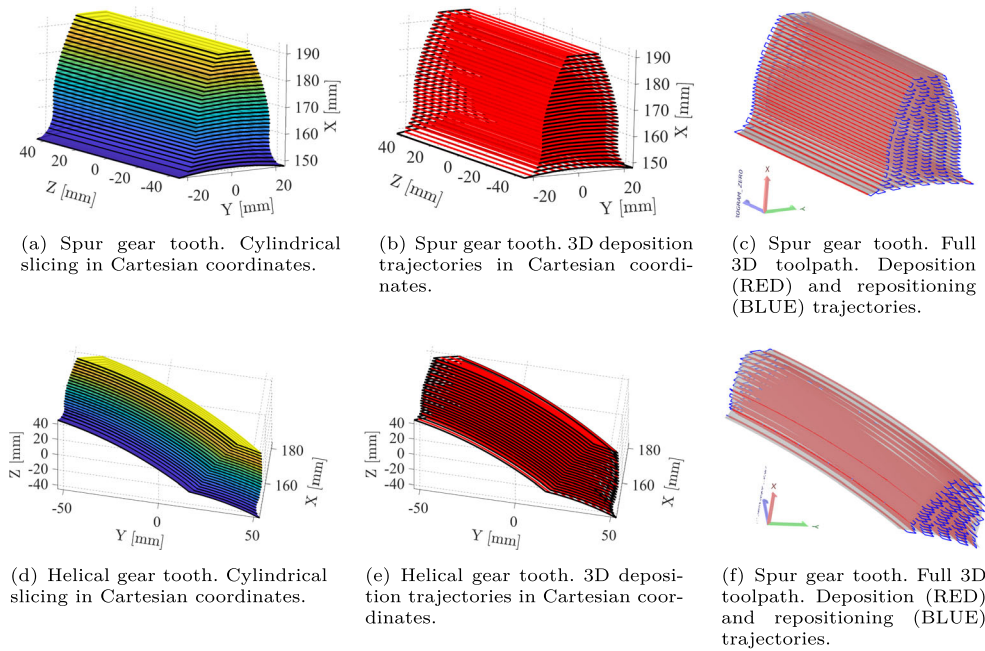


Fig. 11 Experimental validation of our strategy. Spur and helical gears. Cylindrical slicing and 3D toolpath obtained using our approach

2D algorithms and (ii) simple $\mathbb{R}^2 \rightarrow \mathbb{R}^3$ transformations (isometric parametrization) to compute the 3D toolpath.

3.3 Comparison with traditional methods

We manufactured an approximation of a spur gear tooth (Fig. 13a) using traditional (i.e., planar) slicing and 2.5-axis AM. Figure 13b and c show, respectively, the planar layers and the 3D toolpath calculated using our tools for 2.5-axis LMD process planning. To manufacture this workpiece, we used the same experimental setup and process parameters reported in Table 3. We also used a cylindrical substrate of radius 150 mm that simulated the gear shaft. Since, for this experiment, we were using planar slicing, it was necessary to cut, with a secant plane, a piece of the cylinder to produce a planar base. Figure 13d–e show the workpiece obtained by LMD manufacturing. Table 4 informs the number of layers and the building time. It is important to mention that this approximation for building features on cylinders only works when the cutting secant plane is approximately a tangent plane. We cannot use this traditional approach for manufacturing helical gear teeth or propeller blades.

Table 4 Experimental validation. Manufacturing of spur and helical gear teeth. Number of layers and building time

Dataset	Number of layers	Building time (min)
Spur gear tooth (each one)	31	55
Helical gear tooth (each one)	24	46
Spur gear tooth with traditional slicing	35	68

Figure 14 depicts the Vickers hardness curve for (i) the *Sample 5* tooth manufactured with our method for cylindrical slicing and (ii) the tooth manufactured using traditional planar slicing. We measure the hardness along the height of cross-sectional cuts of the teeth. To measure the hardness, we used an FM-300 hardness tester, and we applied a load of 300 g with a dwell time of 12 s. Figure 14 shows that in both cases (planar and cylindrical slicing), the hardness behavior is similar: it is higher near the substrate, and it decreases and stabilizes after certain height (approximately 35 mm in both cases). The hardness is higher near the substrate because the heat dissipates faster (due to conduction) in this region and, therefore, the cooling rate is higher.

3.4 Limitations and prospects of the proposed strategy

The strategy presented in this manuscript addresses the LMD manufacturing of overhanging features on revolution workpieces using cylindrical layers. Our technique does not exclude the simultaneous positioning of the piece and/or LMD dispenser so the dispenser axis is locally normal to

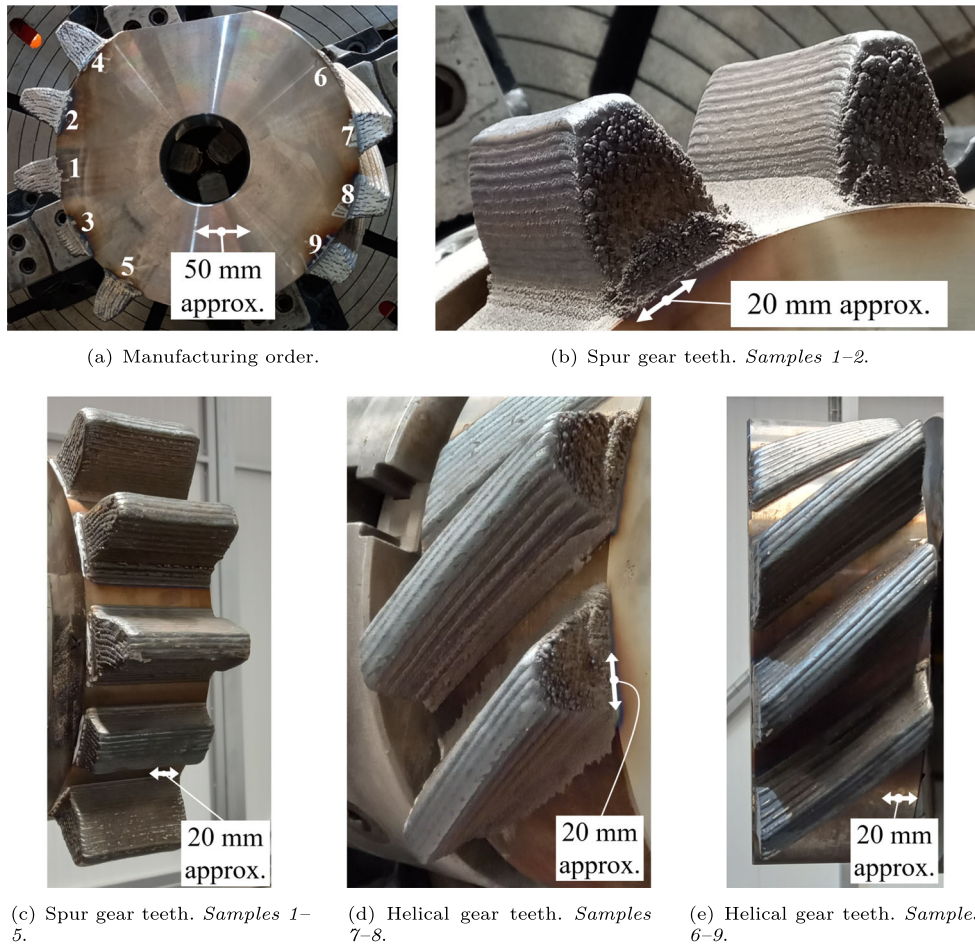


Fig. 12 Experimental validation. LMD manufacturing of spur and helical gear teeth

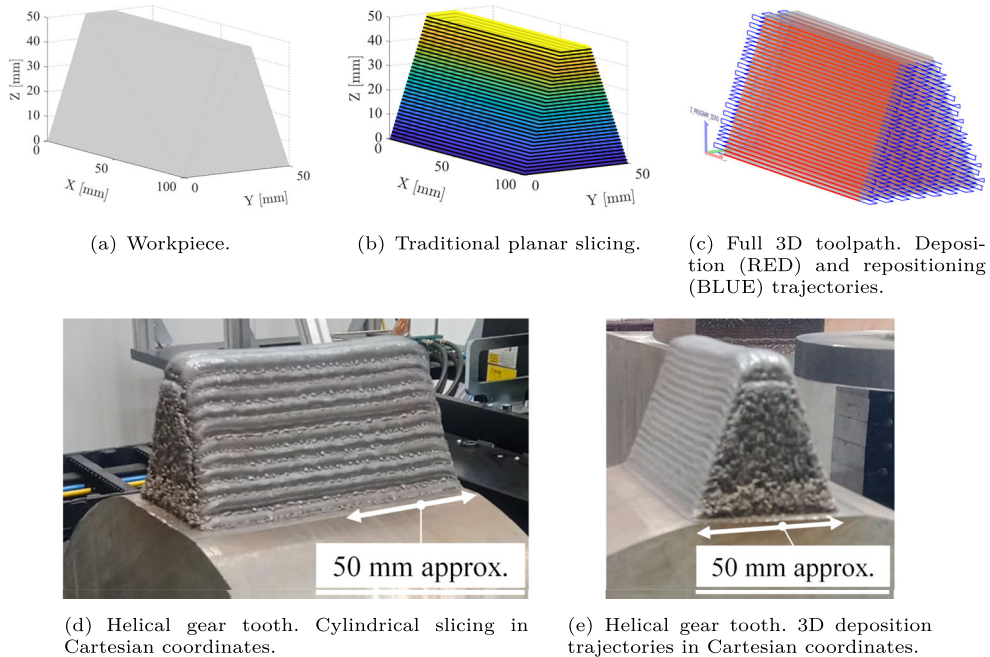


Fig. 13 Traditional (planar) slicing strategy. Approximation of spur gear tooth by coating the gear shaft with a plane

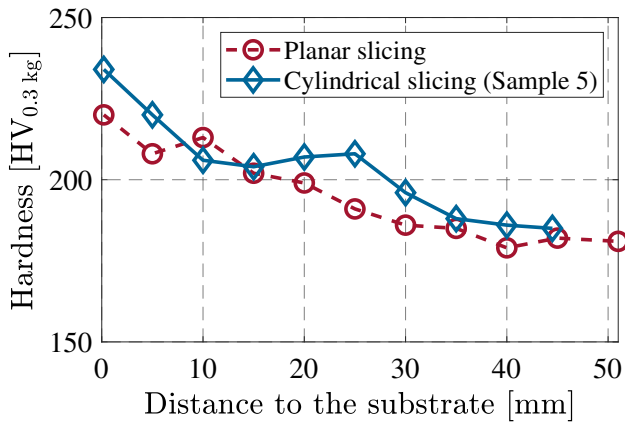


Fig. 14 Hardness measured along the height of the manufactured tooth

the slice surface and aligned with gravity. Such problem is one of inverse kinematics. The examples of this manuscript did not require such instantaneous repositioning, allowing for a constant dispenser orientation. Future work envisions the extension of the current implementation by synchronizing the robot and the rotary plate, achieving the alignment between the nozzle axis, the slice’s local normal vector, and the gravity line during material deposition. This synchronization would provide an additional degree of freedom and allow the manufacturing of more complex workpieces.

The manufacturing of industrial workpieces (using, for example, casting, forging, and additive manufacturing) requires additional processes of surface treatment and finishing. Surface finishing and polishing involve, in many cases, 5-axis CNC machining. For 5-axis finishing of gear teeth in

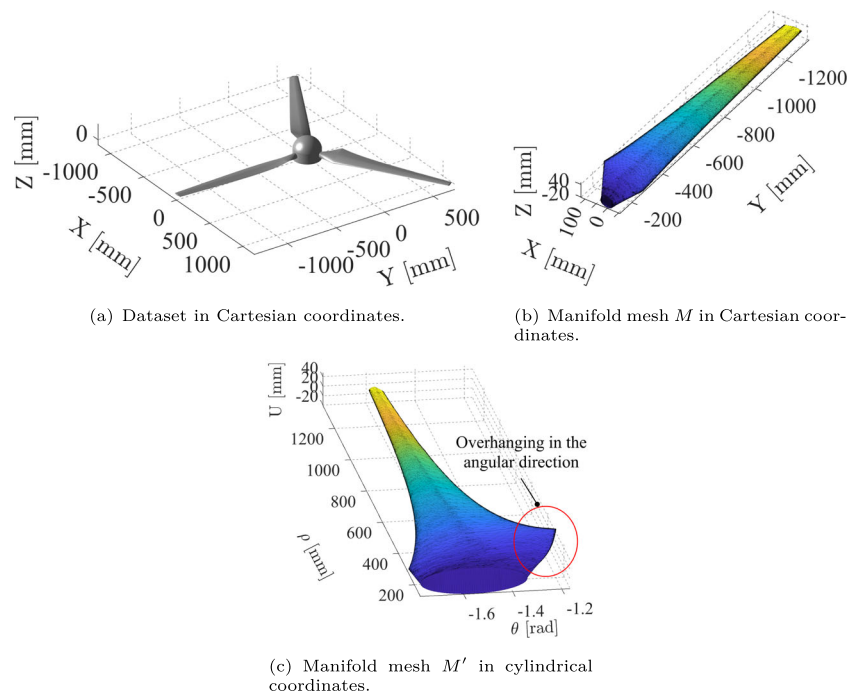
LMD, the interested reader may refer to [29]. This reference addresses the efficient 5-axis machining of flanks using conical tools. Calleja et al. [29] implement an optimization algorithm that approximates the machining surface with conical envelopes, whose shape is determined by the given set of conical tools.

Notice that, regardless of the usage of additive or subtractive manufacturing, gear teeth finishing faces the problems of surface accessibility by the tool.

It is also important to mention that our approach has the following geometrical limitations:

1. Our approach presents limitations when the B-Rep of the overhanging feature \mathcal{M} contains cylinders mounted on a single B-Rep face. If the FACE $\mathcal{F} \subset \mathcal{M}$ is a whole cylinder, the mesh M' (resulting from the transformation of M from Cartesian to cylindrical coordinates) is not 2-manifold. The violation of the 2-manifold condition of M' hinders the use of planar slicing on M' . Geometric modelers usually circumvent this limitation by modeling a whole cylinder with at least 2 FACES.
2. The LMD process discourages the addition of support structures during manufacturing. To fulfill this self-support condition, the 2-manifold \mathcal{M} (or, equivalently, the mesh M) must not have considerable overhanging features in the angular or the axial directions. This condition can be easily analyzed over the mesh M' (transformed version of M in cylindrical coordinates) by checking its overhangs. Figure 15 shows an example of a dataset with considerable overhanging features in the angular direction. Figure 15c shows the manifold mesh

Fig. 15 Wind turbine blade. Overhang in the angular direction. Limitation of our approach



M' associated to the mesh M in Fig. 15b. The presence of overhangs is apparent in this figure. The manufacturing of this workpiece cannot be directly addressed with our strategy.

4 Conclusions

This manuscript presents the implementation and experimental validation of a computer tool for the laser metal deposition (LMD) of overhanging features of revolute workpieces. The implemented strategy for cylindrical slicing and path planning is based on isometric $\mathbb{R}^3 \leftrightarrow \mathbb{R}^2$ transformations and 2.5-axis slicing and path-planning robust algorithms. Our strategy slices the geometry onto (non-planar) iso-radial layers using cylindrical coordinate transformation and planar slicing. Our algorithm generates the toolpath for each iso-radial slice using isometric parametrization (cylinder onto plane, due to cylinder developability) and 2D toolpath-planning methods.

To show the relevance of our algorithm in LMD manufacturing, we compute the toolpath for industrial workpieces: spur and helical gear teeth, and cam lobes. Our LMD path-planner is advantageous because it allows control of the inter-bead (step-over) distance, the dispenser velocity, and the deposited thickness of each iso-radial layer. We manufacture spur and helical gear teeth using an LMD system mounted on a 6-axis robot. The results of the computational and experimental validation show that our algorithm generates toolpaths suitable for LMD manufacturing of industrial workpieces.

Our algorithm has the following limitations: (i) the B-Rep of the workpiece must not contain a cylinder mounted on a single B-Rep FACE, and (ii) the workpiece must not have considerable overhangs in the angular or axial directions to avoid the addition of support structures during manufacturing. Future work will be devoted to alleviate the mentioned limitations.

Funding This work has been partially funded by the Basque Government under ELKARTEK program (grants KK-2018/00115 (ADDISEND) and KK-2018/00071 (LANGILEOK)) and by the INZU Group (Talens Systems and Ikerkune A.I.E.).

Data Availability The data in this study is not available due to industrial secrecy related to this project.

Declarations

Conflict of interest The authors declare that they have no conflicts of interest.

References

1. Leino M, Pekkarinen J, Soukka R (2016) The role of laser additive manufacturing methods of metals in repair, refurbishment and remanufacturing - enabling circular economy. *Phys Procedia* 83:752–760. <https://doi.org/10.1016/j.phpro.2016.08.077>
2. Shan Y, Gan D, Mao H (2021) Curved layer slicing based on isothermal surface. *Procedia Manufacturing* 53:484–491. <https://doi.org/10.1016/j.promfg.2021.06.081>
3. Xu K, Li Y, Chen L, Tang K (2019) Curved layer based process planning for multi-axis volume printing of freeform parts. *Comput Aided Des* 114:51–63. <https://doi.org/10.1016/j.cad.2019.05.007>
4. Dai C, Wang CCL, Wu C, Lefebvre S, Fang G, Liu Y-J (2018) Support-free volume printing by multi-axis motion. *ACM Trans Graph* 37(4):134. <https://doi.org/10.1145/3197517.3201342>
5. Montoya-Zapata D, Moreno A, Ortiz I, Ruiz-Salguero O, Posada J (2022) Cylindrical transform slicing of revolute parts with overhangs for laser metal deposition. In: Posada J, Serrano A (eds) *Spanish Computer Graphics Conference (CEIG)*. The Eurographics Association, Vic, Spain, pp 17–21. <https://doi.org/10.2312/ceig.20221141>
6. Ding Y, Dwivedi R, Kovacevic R (2017) Process planning for 8-axis robotized laser-based direct metal deposition system: a case on building revolved part. *Robot Comput Integr Manuf* 44:67–76. <https://doi.org/10.1016/j.rcim.2016.08.008>
7. Etienne J, Ray N, Panozzo D, Hornus S, Wang CCL, Martínez J, McMains S, Alexa M, Wyvill B, Lefebvre S (2019) CurviSlicer: slightly curved slicing for 3-axis printers. *ACM Trans Graph* 38(4):81. <https://doi.org/10.1145/3306346.3323022>
8. Zhao G, Ma G, Feng J, Xiao W (2018) Nonplanar slicing and path generation methods for robotic additive manufacturing. *The Int J Adv Manuf Technol* 96(9–12):3149–3159. <https://doi.org/10.1007/s00170-018-1772-9>
9. Xie F, Jing X, Zhang C, Chen S, Bi D, Li Z, He D, Tang K (2022) Volume decomposition for multi-axis support-free and gouging-free printing based on ellipsoidal slicing. *Comput Aided Des* 143:103135. <https://doi.org/10.1016/j.cad.2021.103135>
10. Yigit IE, Lazoglu I (2020) Spherical slicing method and its application on robotic additive manufacturing. *Progress in Additive Manufacturing* 5(4):387–394. <https://doi.org/10.1007/s40964-020-00135-5>
11. Eisenbarth D, Menichelli A, Soffel F, Wegener K (2021) Adaptive slicing and process optimization for direct metal deposition to fabricate exhaust manifolds. In: Meboldt M, Klahn C (eds) *Industrializing Additive Manufacturing*. Springer, Cham, pp 160–173. https://doi.org/10.1007/978-3-030-54334-1_12
12. Ruan J, Eiamsa-ard K, Liou FW (2005) Automatic multi-axis slicing based on centroidal axis computation. In: *International Design Engineering Technical Conferences and Computers and Information in Engineering Conference*. Volume 3: 25th Computers and Information in Engineering Conference, Parts A and B, Long Beach, CA, USA, pp 383–393. <https://doi.org/10.1115/DETC2005-85261>
13. Wu C, Dai C, Fang G, Liu Y-J, Wang CCL (2017) RoboFDM: a robotic system for support-free fabrication using FDM. In: 2017 IEEE International Conference on Robotics and Automation (ICRA), pp 1175–1180. <https://doi.org/10.1109/ICRA.2017.7989140>
14. Ding D, Pan Z, Cuiuri D, Li H, Larkin N, van Duin S (2016) Automatic multi-direction slicing algorithms for wire based additive manufacturing. *Robot Comput Integr Manuf* 37:139–150. <https://doi.org/10.1016/j.rcim.2015.09.002>

15. Gao Y, Wu L, Yan D-M, Nan L (2019) Near support-free multi-directional 3D printing via global-optimal decomposition. *Graph Model* 104:101034. <https://doi.org/10.1016/j.gmod.2019.101034>
16. Wu C, Dai C, Fang G, Liu Y-J, Wang CCL (2020) General support-effective decomposition for multi-directional 3-D printing. *IEEE Trans Autom Sci Eng* 17(2):599–610. <https://doi.org/10.1109/TASE.2019.2938219>
17. Xiao X, Joshi S (2020) Process planning for five-axis support free additive manufacturing. *Additive Manufacturing* 36:101569. <https://doi.org/10.1016/j.addma.2020.101569>
18. Xu K, Chen L, Tang K (2019) Support-free layered process planning toward 3 + 2-axis additive manufacturing. *IEEE Trans Autom Sci Eng* 16(2):838–850. <https://doi.org/10.1109/TASE.2018.2867230>
19. Calleja A, Taberner I, Fernández A, Celaya A, Lamikiz A, López de Lacalle LN (2014) Improvement of strategies and parameters for multi-axis laser cladding operations. *Opt Lasers Eng* 56:113–120. <https://doi.org/10.1016/j.optlaseng.2013.12.017>
20. González-Barrio H, Calleja-Ochoa A, López de Lacalle LN, Lamikiz A (2022) Hybrid manufacturing of complex components: full methodology including laser metal deposition (LMD) module development, cladding geometry estimation and case study validation. *Mech Syst Signal Process* 179. <https://doi.org/10.1016/j.ymssp.2022.109337>
21. Xie F, Bi D, Tang K (2020) A potential field based multi-axis printing path generation algorithm. *Int J Comput Integr Manuf* 33(12):1277–1299. <https://doi.org/10.1080/0951192X.2020.1815851>
22. Bi D, Xie F, Tang K (2021) Generation of efficient iso-planar printing path for multi-axis FDM printing. *Journal of Manufacturing and Materials Processing* 5(2):59. <https://doi.org/10.3390/jmmp5020059>
23. Dai F, Zhang H, Li R (2020) Process planning based on cylindrical or conical surfaces for five-axis wire and arc additive manufacturing. *Rapid Prototyping Journal* 26(8):1405–1420. <https://doi.org/10.1108/RPJ-01-2020-0001>
24. Pan S-H, Yao G-C, Cui Y-N, Meng F-S, Luo C, Zheng T-Q, Singh G (2023) Additive manufacturing of tungsten, tungsten-based alloys, and tungsten matrix composites. *Tungsten* 5(1):1–31. <https://doi.org/10.1007/s42864-022-00153-6>
25. Monkova K, Zetkova I, Kučerová L, Zetek M, Monka P, Daňa M (2019) Study of 3D printing direction and effects of heat treatment on mechanical properties of MS1 maraging steel. *Arch Appl Mech* 89(5):791–804. <https://doi.org/10.1007/s00419-018-1389-3>
26. Alomarah A, Zhang J, Ruan D, Masood S, Lu G (2017) Mechanical properties of the 2D re-entrant honeycomb made via direct metal printing. *IOP Conference Series: Materials Science and Engineering* 229(1):012038. <https://doi.org/10.1088/1757-899X/229/1/012038>
27. Montoya-Zapata D, Creus C, Ortiz I, Alvarez P, Moreno A, Posada J, Ruiz-Salguero O (2021) Generation of 2.5D deposition strategies for LMD-based additive manufacturing. *Procedia Computer Science* 180:280–289. <https://doi.org/10.1016/j.procs.2021.01.165>
28. Pressley A (2010) The first fundamental form. In: *Elementary Differential Geometry*. Springer, London, pp 121–157. https://doi.org/10.1007/978-1-84882-891-9_6
29. Calleja A, Bo P, González H, Bartoň M, López de Lacalle LN (2018) Highly accurate 5-axis flank CNC machining with conical tools. *The Int J Adv Manuf Technol* 97(5):1605–1615. <https://doi.org/10.1007/s00170-018-2033-7>

Publisher's Note Springer Nature remains neutral with regard to jurisdictional claims in published maps and institutional affiliations.

Springer Nature or its licensor (e.g. a society or other partner) holds exclusive rights to this article under a publishing agreement with the author(s) or other rightsholder(s); author self-archiving of the accepted manuscript version of this article is solely governed by the terms of such publishing agreement and applicable law.